

THE ISOTHERMAL OUTFLOW IN HIGH-MASS STAR-FORMING REGION G240.31+0.07

JUNHAO LIU and KEPING QIU

School of Astronomy & Space Science, Nanjing University, Nanjing, P.R.China

ABSTRACT

We present Atacama Pathfinder Experiment (APEX) observations toward the massive star-forming region G240.31+0.07 in the CO (3-2), (6-5), and (7-6) lines. The integrated high-velocity and low-velocity emissions of the three lines reveal a bipolar outflow and show similarity in morphology. Using the three CO lines, together with the combined data from the Submillimeter Array (SMA) and the Caltech Submillimeter Observatory (CSO) 10.4 m telescope in CO (2-1), we estimate the physical parameters of the G240.31+0.07 outflow as a function of gas velocity, by the means of large velocity gradient (LVG) modeling and rotation diagram (RD) analysis. Our results reveal that the temperature of the outflow has an almost constant value of ~ 50 K, which is consistent with the isothermal assumption of the wide-angle wind model. We also find a decreasing trend of CO column density with gas velocity. In addition, the modeling results reveal that the outflowing gas is thermalized and no upper limits to the gas density could be derived. The lower limits of gas density are $n_{\text{low}} \sim 10^5 \text{ cm}^{-3}$.

Subject headings: ISM: individual (G240.31+0.07) - ISM: jets and outflows - stars: formation - stars: early-type

1. INTRODUCTION

Molecular outflows are a common phenomenon associated with young stellar objects (YSOs) of all masses (Lada 1985; Fukui et al. 1993; Zhang et al. 2001; Beuther et al. 2002; Maud et al. 2015). In sites of low-mass star formation, molecular outflows involve amounts of energy similar to those involved in the accretion processes and are indispensable for dissipating excess angular momentum of accretion disks (Shu et al. 1987; Bachiller 1996). Thus, outflows are a fundamental part of the formation process of low mass stars. Due to the rarity and typically larger distances, the case of massive molecular outflows is more problematic than their low-mass counterparts. Many questions, e.g., how the massive outflows are accelerated, how they differ from low-mass outflows, and how they affect the high-mass star-forming processes, are still unanswered. It is essential to address these questions by studying individual outflows associated with high-mass star-forming regions.

Most previous studies of outflows have used low-J transitions of CO, which are easily excited at low temperatures, to characterize the relatively cold molecular gas in morphology and kinematics (Qiu et al. 2009; Qiu & Zhang 2009; Qiu et al. 2011). Observations of high-J CO lines, which probe the warm gas, are very rare. To derive the physical parameters of the outflowing gas, sensitive observations of CO across multiple transitions are needed.

Here we report the 12-m submillimeter Atacama Pathfinder Experiment Telescope¹ (APEX) observations of G240.31+0.07 (hereafter G240), an active high-mass star-forming region which is associated with the young stellar object (YSO) IRAS 07427-2400 and located at a distance of 5.41 kpc (Sakai et al. 2015). It harbors an ultracompact HII region and is associated with OH and

¹The Atacama Pathfinder Experiment Telescope is a collaboration between the Max-Planck-Institut für Radioastronomie, the European Southern Observatory, and the Onsala Space Observatory.

H₂O masers (Hughes & MacLeod 1993; Caswell 1997; MacLeod et al. 1998; Migenes et al. 1999; Caswell 2003). Its far-infrared luminosity of $10^{4.7} L_{\odot}$ is consistent with a spectral type O8.5 zero-age main-sequence star (MacLeod et al. 1998). A near-infrared study has found two bright elongated H₂ emission knots near the source (Kumar et al. 2002). Kumar et al. (2003) further argued that the shocked H₂ emission indicates the presence of a massive rotating disk/envelope around the luminous YSO IRAS 07427-2400.

There are also millimeter and centimeter radio continuum observations toward G240. Two clumps were detected by Chen et al. (2007) at 654 GHz (460 μ m), with clump A coinciding with a VLA 6 cm point source (Hughes & MacLeod 1993) and an H₂O maser. Qiu et al. (2009) presented a high resolution interferometric study at 1.3 mm and resolved the central part of G240 into three dusty cores MM1, MM2, and MM3, with the brightest core MM1 coinciding with the VLA 6 cm point source spatially. Trinidad (2011) presented observations at 1.3, 3.6, and 6 cm and reported radio continuum emissions at the position of the three millimeter sources in at least one wavelength.

G240 has also been mapped with single dish and interferometric observations in CO emission. High-velocity CO (1-0) gas was detected towards G240 (McCutcheon et al. 1991; Shepherd & Churchwell 1996), tracing a bipolar outflow (Shepherd & Churchwell 1996). Hunter (1997) mapped the CO (3-2) emission with a 20'' beam and found a prominent bipolar outflow at a position angle (PA) of 138° and a weaker component at PA \sim 101°. Kumar et al. (2003) also detected a prominent component and a weaker component of the bipolar CO (3-2) outflow with a 20'' beam and reported the PA of the prominent component to be 132°. Recently, Qiu et al. (2009) presented a detailed single dish and interferometric study of ¹²CO(2-1) and ¹³CO(2-1) emission and detected a bipolar, wide-angle, quasi-parabolic molecular outflow.

In addition, Qiu et al. (2014) reported the detection of an hourglass magnetic field aligned within 20° of the outflow axis.

In this paper, we present a CO multi-transition (3-2, 6-5, 7-6) study towards the G240 outflow. With large velocity gradient (LVG) calculations

and population diagram analysis, we estimate the physical parameters of the outflow as a function of gas velocity. We then discuss the results of the analysis.

2. OBSERVATIONS

The APEX observations were conducted on . CO (6-5) and CO (7-6) were observed simultaneously. The pointing error was found to be and we have fixed it.

3. RESULTS

3.1. CO EMISSIONS AND LINE RATIOS

The cloud velocity (v_{cloud}) with respect to the local standard of rest is about 67.5 km s⁻¹, which is adopted from Kumar et al. (2003). Figure 1 shows the integrated low-velocity (LV) and high-velocity (HV) emissions of CO J = (2-1), (3-2), (6-5), (7-6). The outflow morphologies seen in CO (3-2), (6-5) and (7-6) are very similar. For the three lines detected by APEX, a prominent bipolar outflow at (PA) \sim 131° along with a weaker component at PA \sim 101° is detected. The weaker component is at relatively lower velocities, while the prominent component is detected at both low and high velocities. The signal-to-noise ratio in the CO (7-6) spectrum is relatively low at high velocities. Overall, the CO (3-2), (6-5), (7-6) maps presented in Figure 1 are very similar to the CO (3-2) map presented by Kumar et al. (2003). Due to angular resolution, the CO J = (3-2), (6-5), (7-6) emissions don't show the wide-angle structure highlighted by the CO (2-1) emission.

To compare the emissions of different CO transitions, we convolved the CO (2-1), (6-5) and (7-6) maps, to the same spatial resolution of the CO (3-2), which is 19''. To reduce the noise level in the spectra, we resampled the four CO lines to a resolution of 2 km s⁻¹. Then we measured the main beam temperature (T_{mb}) of different CO lines at the peak of the blueshifted and the redshifted lobes (marked as two crosses in each panel of Figure 1). Figure 2 shows the observed line wing ratios of different CO transitions. All line ratios in Figure 2 are remarkably constant with velocity.

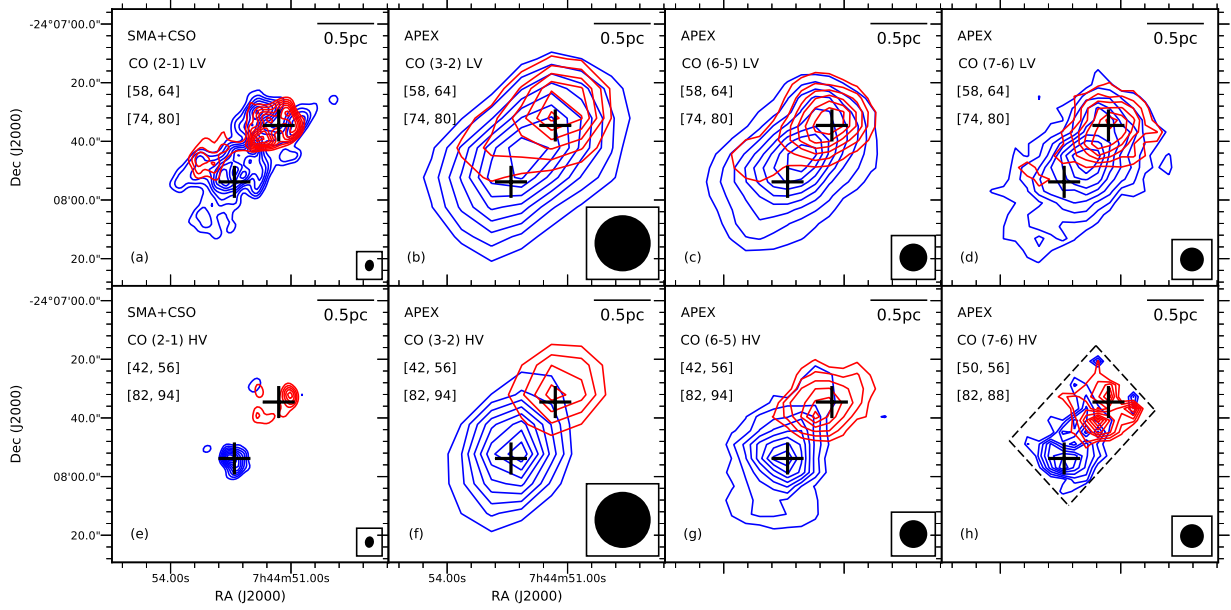


Fig. 1.— (a)-(d) Low-velocity CO $J = (2-1), (3-2), (6-5), (7-6)$ emissions, integrated from 58 to 64 km s^{-1} for the blueshifted lobe (blue) and from 74 to 80 km s^{-1} for the redshifted lobe (red); (e)-(g) High-velocity CO $J = (2-1), (3-2), (6-5)$ emissions, integrated from 42 to 56 km s^{-1} for the blueshifted lobe (blue) and from 82 to 94 km s^{-1} for the redshifted lobe (red); (h) High-velocity CO $J = (7-6)$ emission, integrated from 50 to 56 km s^{-1} for the blueshifted lobe (blue) and from 82 to 88 km s^{-1} for the redshifted lobe (red). For (a)-(g), the contour levels start from 20% and continue at steps of 10% of the peak emission. For (h), the contour levels start from 30% and continue at steps of 10% of the peak emission. The central stars mark the positions of the millimeter sources detected by Qiu et al. (2009). The beam size is shown in the lower right corner of each panel. The CO (2-1) maps are adopted from Qiu et al. (2009).

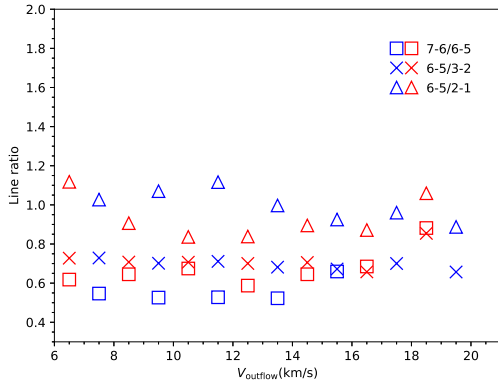
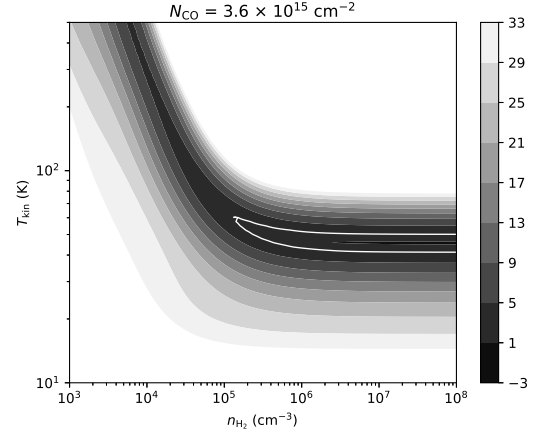


Fig. 2.— Ratios of the T_{mb} of different CO lines at different velocities. Blue symbols denote the measurements from the blueshifted lobe, and red symbols the redshifted lobe. The V_{outflow} shown here is related to the v_{cloud} by the relation: $V_{\text{outflow}} = |v_{\text{outflow}} - v_{\text{cloud}}|$, where v_{outflow} is the outflow velocity with respect to the local standard of rest.

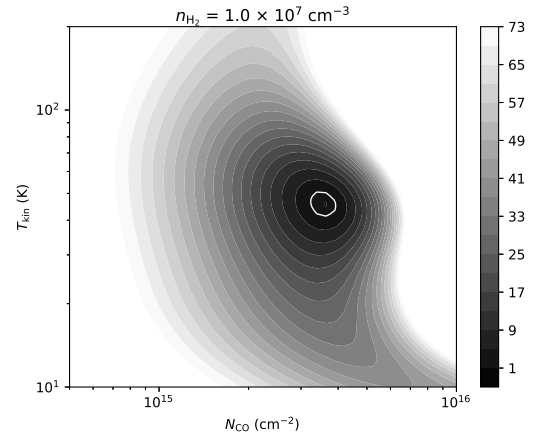
3.2. PHYSICAL PROPERTY ANALYSIS

Because the ^{13}CO emission is not detected in the outflowing gas, the four transitions of ^{12}CO are assumed to be optically thin during our analysis. Using the RADEX code (van der Tak et al. 2007), we construct a large grid of non-LTE models with three parameters: gas density (n_{H_2}), kinetic temperature (T_{kin}), and CO column density (N_{CO}). Linewidths are given as input and are fixed to 2 km s^{-1} . The physical parameters in the outflow can be derived by comparing the main beam temperatures of various transitions with the model line intensities. Because of the degeneracies of the source size with the CO column density (in the optically thin case), all the computations are done with the assumption that the beam-filling factor is one for each transition. Thus, the derived physical parameters are beam-averaged values. The best fit is obtained by minimizing the χ^2 between the observed data and the model intensities. During the fitting, the intensity uncertainties of CO (2-1), CO (3-2), CO (6-5), CO (7-6) are set to 0.15, 0.2, 0.25, 0.3 respectively.

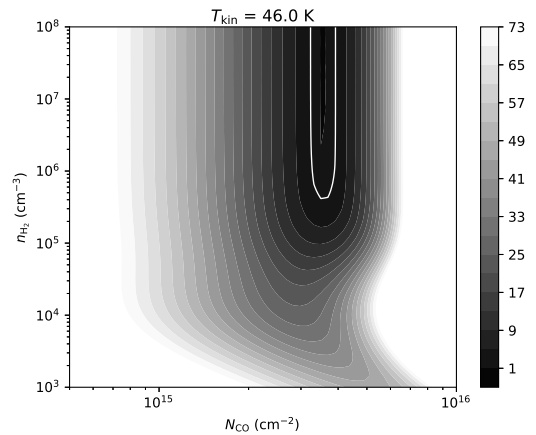
We also perform a rotation diagram (RD) analysis (Goldsmith & Langer 1999). Throughout the



(a)



(b)



(c)

4 Fig. 3.— The χ^2 distribution for G240 outflow at 82 km s^{-1} in the (a) $[T, n]$, (b) $[T, N]$, (c) $[n, N]$ planes, with all other parameters fixed to the parameters of the best fitting results at this velocity. Solid contours show the 1σ confidence levels.

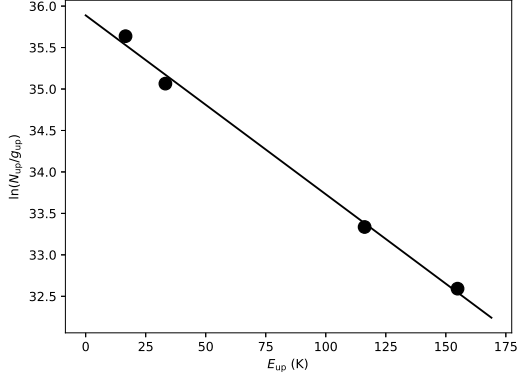


Fig. 4.— Population diagram for CO at 82 km s⁻¹. The fitted line shows the Boltzmann distribution of the rotational populations.

RD analysis, we assume that the outflow emission is optically thin and that the excitation of the sub-levels is close to LTE. The population of each level is given by

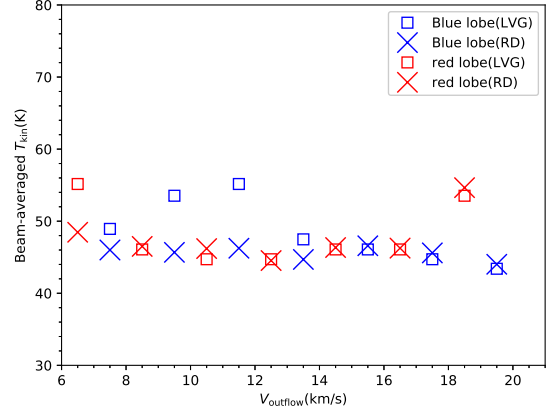
$$N_{\text{up}} = \frac{N_{\text{CO}}}{Z} g_{\text{up}} e^{-E_{\text{up}}/kT_{\text{kin}}}, \quad (1)$$

where N_{up} is the column density in the upper state, g_{up} the statistical weight of the upper state, E_{up} the upper energy level, k the Boltzmann constant, and Z is the partition function. RD for CO at 82 km s⁻¹ as an example is shown in Figure 4. The molecular energy levels are in Boltzmann distribution. The RD behaves similarly at other velocities.

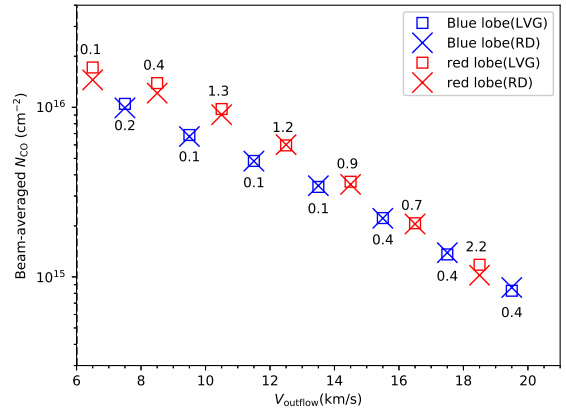
Figure 5 shows the outflowing gas temperature and the CO column density, estimated from the LVG analysis and the RD analysis, as functions of gas velocity. The N - V diagram shows a clear decreasing trend of CO column density with outflow velocity, while the T - V diagram shows that the gas temperature has no obvious dependence on gas velocity. The χ^2 calculated from the LVG analysis are shown in Figure 5(b).

3.3. ERROR OF THE FITTED PARAMETERS

With four line observations and three simulation parameters, our fitting has one degree of freedom. Thus, the value of the reduced chi-square (χ^2_{red}) equals the value of the χ^2 . As shown in



(a)



(b)

Fig. 5.— T - V and N - V diagrams of the G240 outflow, estimated from LVG analysis (blue open squares for blue lobe and red open squares for red lobe) and RD analysis (blue x marker for blue lobe and red x marker for red lobe). The χ^2 calculated from the LVG analysis are shown in the N - V diagram.

Figure 5(b), the best fitting results at most velocities have a χ_{red}^2 that is less than 1, indicating that our adopted calibration error may be a bit conservative or the real value of degrees of freedom is smaller than one (Andrae et al. 2010). In Figure 3, we show cuts in the χ^2 along the $[T, n]$, $[T, N]$, $[n, N]$ planes at 82 km s^{-1} , with all the other parameters fixed to the parameters of the best fitting result at this velocity, as examples of the χ^2 distribution. As shown in Figure 3(b), the χ^2 has only one minimum in $[T, N]$ planes. However, Figure 3(a) and Figure 3(c) show that the gas is thermalized and no upper limits to the density could be derived. The χ^2 distribution behaves similarly at other velocities.

We derive the uncertainties of each parameter of the LVG analysis from the 1σ confidence region in the N - T - n 3-dimensional space at velocities where $\chi_{\text{red}}^2 \sim 1$. The 1σ confidence range of temperature is about 40 K - 60 K. The lower limit of gas density (n_{lower}) is around 10^5 cm^{-3} . The uncertainty of the CO column density is $\sim 10 \%$.

4. DISCUSSION

4.1. Temperature

The LVG analysis and the population diagram analysis reveal that the G240 outflow has almost constant temperatures of $\sim 50 \text{ K}$. This value is consistent with temperatures in excess of 50 K probed by van Kempen et al. (2016) for outflows associated with intermediate-mass protostars, and slightly lower than temperatures of outflows associated with low-mass protostars (van Kempen et al. 2009; Yıldız et al. 2012).

The $T - V$ relation of outflows have been studied by several authors. A rising CO 3-2/6-5 ratio is observed towards the outflow associated with low-mass YSO HH46 (van Kempen et al. 2009). With the density assumed to be constant, the rising ratios at more extreme velocities correspond to lower kinetic temperatures. In the case of the outflow associated with low-mass protostars NGC 1333 IRAS 4A and IRAS 4B, the CO 3-2/6-5 ratios are remarkably constant with velocity (Yıldız et al. 2012). With the assumption of constant density, the constant ratios indicate constant temperatures. Su et al. (2012) have imaged the extremely high velocity (EHV) outflow in CO (2-1) and CO (3-2) associated with the high-mass YSO G5.89-

0.39. With the assumption of a canonical CO fractional abundance of 10^{-4} , an increasing trend of temperature with outflow velocity is found by performing a LVG analysis. However, using the CO (6-5), (7-6) and (16-15) lines, Leurini et al. (2015) performed a rotation diagram analysis towards G5.89-0.39 outflow and found a decreasing trend of temperature with increasing velocities. This disagreement seen in results of Su et al. (2012) and Leurini et al. (2015) could be due to different angular resolutions ($3''.4$ compared to $14''.5$). While Su et al. (2012) has smaller energy range covered by their CO line observations ($\Delta E_u \sim 17 \text{ K}$) compared to $\Delta E_u \sim 600 \text{ K}$ of Leurini et al. (2015), the decreasing trend of temperature with velocity constrained in Leurini et al. (2015) is probably more appropriate for the G5.89-0.39 outflow. The different $T - V$ relations found in different outflows and in different angular scales reveal the complexity of molecular outflows.

In the wide-angle wind model, a molecular outflow is the ambient material swept-up by a wide-angle radial wind. In previous numerical works, many authors chose isothermal equations for this model (Li & Shu 1996; Lee et al. 2001). Molecular cooling dominates the cooling of the shocked material in the outflow at temperatures below 10^4 K (Hollenbach 1997). As the cooling rate increases as n^2 , molecular cooling is very efficient for the density of a wind-driven outflow. Thus, an isothermal state could be reached in a wind-driven outflow, with no temperature change with velocity. This is consistent with our derivation of almost constant temperature in the massive G240 outflow. In addition, some other features of the molecular outflow associated with G240 can also be qualitatively interpreted by the wide-angle wind model (Qiu et al. 2009), while other outflow models have different predictions of these features (Arce et al. 2007). However, most outflow models existed have parameters typical of low-mass outflows. It is necessary to compare the observational results of high-mass outflows with models of similar physical conditions. Statics of outflows associated with high-mass star-forming regions are also essential for us to better understand the driven mechanism of massive outflows and the forming process of high-mass stars.

4.2. Density

The LVG analysis reveals that the lower limits of gas densities are $\sim 10^5 \text{ cm}^{-3}$ at most velocities. We have found a decreasing trend of the beam averaged CO column density ($N_{\text{CO,beam}}$) with gas velocity. As shown in Figure 5(b), for each velocity bin, the beam averaged CO column density drops from $\sim 10^{16} \text{ cm}^{-2}$ to $5 \times 10^{14} \text{ cm}^{-2}$ within 15 km s^{-1} . In the optically thin case, the beam averaged CO column density could be related to gas density n_{H_2} :

$$N_{\text{CO,beam}} = n_{\text{H}_2} \times \Delta V \times \frac{1}{dv/dr} \times X_{\text{CO}} \times f_b, \quad (2)$$

where f_b is the beam filling factor, X_{CO} the CO/H₂ abundance ratio, ΔV the velocity interval and dv/dr is the velocity gradient. A drop in $N_{\text{CO,beam}}$ at more extreme velocities indicates the decrease of one or several of these parameters. To explore how the effect of beam dilution influence our results, we varied the beam filling factors from 0.2 to 1. Then we performed the LVG analysis again, and compared the simulated T_b with the corrected antenna temperatures (T_{mb} divided by a beam filling factor). We find that modelling with different beam filling factors mainly affect the N - V diagram, with minor change in the T - V diagram and density limits. This could be resulted from the degeneracies of the beam filling factor with CO column density in the optically thin case.

As shown in Figure 3 of Qiu et al. (2009), the source size are $\sim 20''$ and $\sim 10''$ at velocities of $\sim \pm 6 \text{ km s}^{-1}$ and $\sim \pm 20 \text{ km s}^{-1}$ with respect to the cloud velocity, corresponding to beam filling factors of ~ 0.5 and ~ 0.2 , respectively. Considering the 2.5 times drop in the beam filling factor, the 20 times drop in the beam averaged CO column density is consistent with ~ 8 times decrease in the CO column density. As shown in Shu et al. (1995), estimation from an x-wind model predict the wind density decreasing with velocity and distance from the driving source. Thus, the decrease of gas density could interpret the decrease of CO column density with velocity. Due to the lack of further informations, we cannot assess whether the CO abundance ratio or the velocity gradient has attributed to the drop of CO column density at high velocities.

5. SUMMARY

We have presented a CO multi-transition study towards the molecular outflow of the high-mass star-forming region G240. With the LVG analysis, we have constrained the temperatures to $\sim 50 \text{ K}$ and the H₂ density to values higher than $n \sim 10^5 \text{ cm}^{-3}$. We also find a decreasing trend of CO column density with gas velocity.

REFERENCES

- Andrae, R., Schulze-Hartung, T., & Melchior, P. 2010, arXiv:1012.3754
- Arce, H. G., Shepherd, D., Gueth, F., et al. 2007, *Protostars and Planets V*, 245
- Bachiller, R. 1996, *ARA&A*, 34, 111
- Beuther, H., Schilke, P., Sridharan, T. K., et al. 2002, *A&A*, 383, 892
- Caswell, J. L. 1997, *MNRAS*, 289, 203
- Caswell, J. L. 2003, *MNRAS*, 341, 551
- Chen, H.-R., Su, Y.-N., Liu, S.-Y., et al. 2007, *ApJ*, 654, L87
- Fukui, Y., Iwata, T., Mizuno, A., Bally, J., & Lane, A. P. 1993, *Protostars and Planets III*, 603
- Goldsmith, P. F., & Langer, W. D. 1999, *ApJ*, 517, 209
- Hollenbach, D. 1997, *Herbig-Haro Flows and the Birth of Stars*, 182, 181
- Hughes, V. A., & MacLeod, G. C. 1993, *AJ*, 105, 1495
- Hunter, T. R. 1997, *Ph.D. Thesis*, 238
- Kumar, M. S. N., Bachiller, R., & Davis, C. J. 2002, *ApJ*, 576, 313
- Kumar, M. S. N., Fernandes, A. J. L., Hunter, T. R., Davis, C. J., & Kurtz, S. 2003, *A&A*, 412, 175
- Lada, C. J. 1985, *ARA&A*, 23, 267
- Lee, C.-F., Stone, J. M., Ostriker, E. C., & Mundy, L. G. 2001, *ApJ*, 557, 429

- Leurini, S., Wyrowski, F., Wiesemeyer, H., et al. 2015, *A&A*, 584, A70
- Li, Z.-Y., & Shu, F. H. 1996, *ApJ*, 472, 211
- MacLeod, G. C., Scalise, E., Jr., Saedt, S., Galt, J. A., & Gaylard, M. J. 1998, *AJ*, 116, 1897
- Maud, L. T., Moore, T. J. T., Lumsden, S. L., et al. 2015, *MNRAS*, 453, 645
- McCutcheon, W. H., Sato, T., Dewdney, P. E., & Purton, C. R. 1991, *AJ*, 101, 1435
- Migenes, V., Horiuchi, S., Slysh, V. I., et al. 1999, *ApJS*, 123, 487
- Qiu, K., Zhang, Q., Wu, J., & Chen, H.-R. 2009, *ApJ*, 696, 66
- Qiu, K., & Zhang, Q. 2009, *ApJ*, 702, L66
- Qiu, K., Zhang, Q., & Menten, K. M. 2011, *ApJ*, 728, 6
- Qiu, K., Zhang, Q., Menten, K. M., et al. 2014, *ApJ*, 794, L18
- Sakai, N., Nakanishi, H., Matsuo, M., et al. 2015, *PASJ*, 67, 69
- Shepherd, D. S., & Churchwell, E. 1996, *ApJ*, 457, 267
- Shu, F. H., Adams, F. C., & Lizano, S. 1987, *ARA&A*, 25, 23
- Shu, F. H., Najita, J., Ostriker, E. C., & Shang, H. 1995, *ApJ*, 455, L155
- Su, Y.-N., Liu, S.-Y., Chen, H.-R., & Tang, Y.-W. 2012, *ApJ*, 744, L26
- Trinidad, M. A. 2011, *AJ*, 142, 147
- van der Tak, F. F. S., Black, J. H., Schöier, F. L., Jansen, D. J., & van Dishoeck, E. F. 2007, *A&A*, 468, 627
- van Kempen, T. A., van Dishoeck, E. F., Güsten, R., et al. 2009, *A&A*, 501, 633
- van Kempen, T. A., Hogerheijde, M. R., van Dishoeck, E. F., et al. 2016, *A&A*, 587, A17
- Yıldız, U. A., Kristensen, L. E., van Dishoeck, E. F., et al. 2012, *A&A*, 542, A86
- Zhang, Q., Ho, P. T. P., Wright, M. C. H., & Wilner, D. J. 1995, *ApJ*, 451, L71
- Zhang, Q., Hunter, T. R., Brand, J., et al. 2001, *ApJ*, 552, L167